Contents lists available at ScienceDirect

Computational Materials Science

Effects of topological point reconstructions on the fracture strength and deformation mechanisms of graphene

Matthew Daly, Meaghan Reeve, Chandra Veer Singh *

Department of Materials Science and Engineering, University of Toronto, 184 College Street, Suite 140, Toronto, Ontario M5S 3E4, Canada

ABSTRACT

Recent experimental studies have identified a number of topological reconstructions of point defects in graphene, however, their influence on fracture strength has not been studied. From a weakest-link perspective, each of these defects are potentially strength-limiting features, necessitating investigation of their effects on mechanical properties. In the present study, molecular dynamics tensile simulations are performed to quantify the strengths of single and divacancy topological reconstructions with consideration of temperature and strain rate effects. Fracture strengths in the range of 92–101 GPa are obtained for the topological reconstructions at 300 K and a strain rate of 10^9/s. This range shifts to 81–95 GPa when the loading rate is decreased to 5×10^6/s, highlighting the significant influence of kinetic factors on fracture strength. Similarly, an increase in temperature causes appreciable strength reductions, resulting in fracture strengths of 87–97 GPa at 450 K and a 10^9/s strain rate. In order to provide a meaningful comparison to the limited experimental data available, the energy barriers for fracture are determined from thermal activation theory. Analytical calculations predict fracture strengths in the range of 50–79 GPa at 300 K and 10^0/s, which agrees well with experimental reports. Surprisingly, the topological point reconstructions with under-coordinated atoms and highest potential energies are found to be the strongest defects. Physically, under-coordinated atoms are observed to undergo bond rotations, enabling a deformation accommodation mechanism that suppress brittle fracture and leads to improved flaw tolerance. This finding is supported by Quantized Fracture Mechanics calculations.

© 2014 Elsevier B.V. All rights reserved.

1. Introduction

Large-scale synthesis of graphene, *e.g.* by chemical vapor deposition [1–5], is well known to introduce a number of imperfections such as point [6] and line defects [7,8] into its topological structure. Typically, defects are ubiquitous in bulk materials and represent structural flaws that compromise mechanical properties by leading to premature failure. In 2D systems, such defects transcend the entire material thickness, raising significant concerns regarding their impact on strength. Unlike metallic crystals, graphene possesses a number of different observed topological point defects which are formed as reconstructions from bond rotations [9,10], and single [9,10] and divacancies [10]. These topological structures possess low formation energies in the range of 4.5–7.9 eV [11] and represent the energy minimized structures of vacancy defects, which are expected to reconstruct spontaneously during material service. Atomic-scale studies of graphene and conventional graphite

have shown that single vacancy (SV) defects reconstruct into a pentagon–nonagon pair [9,10,12], whereas the divacancy (DV) defect may reorganize into several geometric allotropes [11,13]. Previous investigations have identified two different critical low energy DV allotropes, namely, the pentagon–octagon–pentagon (DV^1) [10,14,15] and the quad-pentagon–hexagon–quad-heptagon (DV^2) [10] topological reconstructions.

Currently, mechanical testing of graphene membranes is largely restricted to atomic force microscopy (AFM) nanoindentation studies [16–20]. Experimental investigations of the impact of point defects on mechanical properties is limited to a study of strength deterioration resulting from oxygenation and pore formation of plasma-etched graphene membranes [20]. However, the topological structure of defects in this study was not reported. In lieu of direct experiments, atomistic simulations of defects in graphene have witnessed significant research attention, with a number of recent studies aimed at predicting the mechanical properties of defective structures. For example, the Stone–Wales defect is a well known topological point reconstruction in graphene that has been shown in a number of rigorous computational studies to have a relatively minor impact on mechanical strength [21–27].

* Corresponding author. Tel.: +1 416 946 5211; fax: +1 416 978 4155.
E-mail address: chandraveer.singh@utoronto.ca (C. Veer Singh).

Although insightful, atomistic studies have typically been utilized to quantify intrinsic mechanical properties, making comparisons to experimental data notably difficult. Molecular dynamics (MD) studies, for example, are often limited to mechanical testing at very large strain rates. The influence of kinetic factors are therefore notably difficult to quantify using direct atomistic approaches. In order to circumvent the limitations of atomistic studies, thermal activation theory [28] may be used in combination with atomistic simulations to provide more accurate comparisons to experimental data. With the implications of strain rate sensitivity in mind, a number of researchers have used atomistic simulations to investigate the influence of elliptical nano-cracks on fracture strength [25,29,30] and the energy barriers resisting fracture in the Stone–Wales defect [25,27], as well as fracture propagation in graphene with edge cracks [31]. Additionally, investigators have examined strain rate sensitivity in graphene tilt boundaries [32–34]. These works show a significant strength decrease in pristine graphene resulting from the presence of atom-scale flaws, with the degree of weakening found to increase as strain rates approach experimental ranges [34]. This highlights the influence thermally activated deformation processes can have on strength, motivating a thorough examination of the coordinated point reconstructions.

In comparison to the Stone–Wales defect, investigation of the SV and DV topological reconstructions is somewhat limited in the literature. Ansari et al. [26] studied the mechanical properties of the SV defect using direct MD simulations. In this work, the investigators show that the SV defect has a relatively minor impact on pristine strength. Similar behavior was reported in a separate computational study of SV defects in graphene [23,25]. The scope and applicability of these findings to experimental data are limited, however, as strain rate effects were not considered. With respect to the DV reconstructions, Dettori et al. [35] studied the effect of defect concentration on the elastic modulus of DV^1 defective graphene membranes. Additionally, the electronic structure and vacancy migration of behavior of DV defects have been examined [36,37]. Fracture strengths of the DV^1 and DV^2 reconstructions, however, have not been reported so far despite being observed experimentally alongside the SV defect [9,10] and having formation energies comparable to the SV reconstruction [11]. From a weakest-link perspective, both the SV and DV reconstructions may be expected to cause premature failure in graphene. A comparative mechanical study of the common topological point reconstructions is therefore critical to understanding the mechanical limitations of defective graphene. In order to provide a meaningful comparison of the topological reconstructions, the influence of strain rate effects on mechanical strength must also be considered. The purpose of the current work is therefore to perform a comparative mechanical analysis of the SV, DV^1, and DV^2 defects. MD tensile simulations are used to determine fracture strength of defective graphene samples and kinetic effects are quantified by varying strain rates and temperature. The physical phenomena underpinning measurements of strength are investigated through a detailed examination of evolving crack morphologies during fracture.

2. Computational modeling

MD tensile simulations were performed using LAMMPS [38] and interatomic interactions were modeled using the AIREBO [39] potential with a bond cut-off radius of 1.92 Å. This cut-off distance has been previously validated with density functional theory tensile simulations of graphene [40]. Graphene samples measuring 64 nm^2 were created for MD testing under periodic boundary conditions. A schematic of the MD simulation cell is provided in Fig. 1. Each of the reconstructions were created by injecting the required number of vacancies into the graphene sheet and then rotating
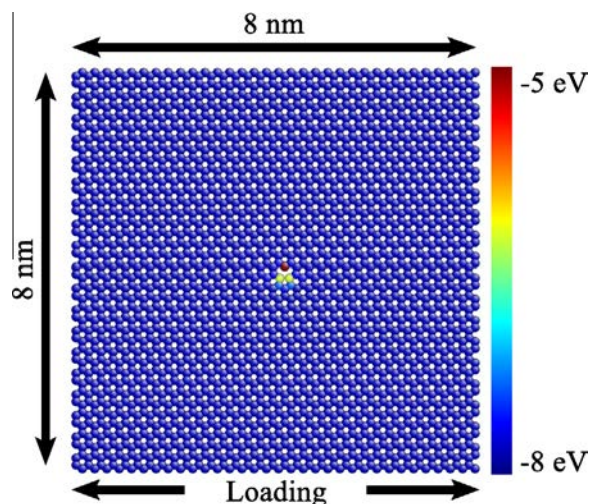

Fig. 1. A typical MD simulation cell used in tensile deformation of the reconstructed SV defect, which was positioned near the centre of the cell. The color mapping indicates per atom potential energies. The loading direction for MD tensile simulations is also indicated. (For interpretation of the references to color in this figure legend, the reader is referred to the web version of this article.)

existing bonds into their reconstructed topologies. Fig. 2 provides the topologies of the SV, DV^1, and DV^2 defects which were analyzed in this study. As shown in the figure, the SV reconstruction
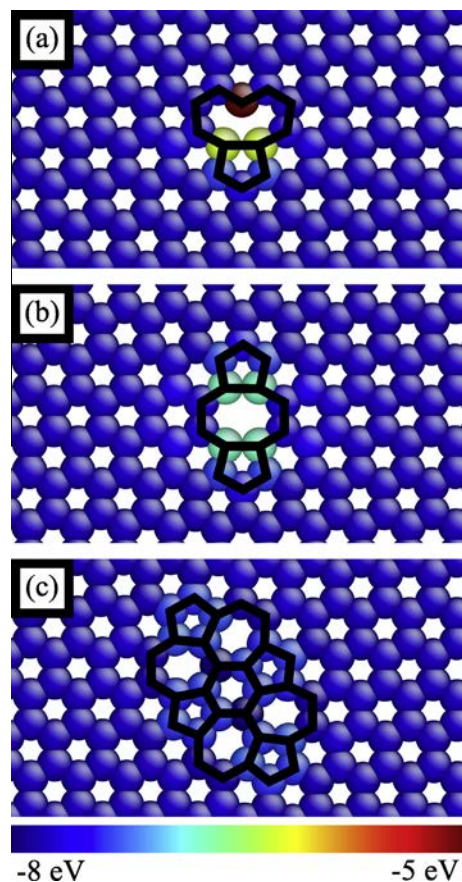

Fig. 2. Atomic topologies of the (a) SV, (b) DV^1, and (c) DV^2 reconstructions. The colormap indicates per atom potential energies. The DV^2 structure had the lowest potential energy of all the topological point reconstructions. (For interpretation of the references to color in this figure legend, the reader is referred to the web version of this article.)

possessed atoms with the highest potential energies in the defect core, in part from the presence of an under-coordinated atom in the irregular-nonagon. Although fully coordinated under zero load, the DV^1 defect was composed of a number of higher energy atoms due to the large bond angle within the octagon. In general, the high energy atoms in the SV and DV^1 defects were susceptible to bond-breakage and subsequent under-coordination during tensile simulation. In contrast to the SV and DV^1 structures, the DV^2 reconstruction was comprised of a fully coordinated topology with low energy bond pairings.

Prior to tensile loading, defective graphene sheets were subjected to conjugate gradient minimization and relaxation to ensure a ground-state system energy and near-zero pressure. In order to understand strain rate effects, uniaxial tensile testing was performed at strain rates in the range of 5×10^6 to 10^9/s. Uniaxial loading was applied along the zigzag direction (see Fig. 1) and system temperature (T) was maintained using the Nose–Hoover isothermal–isochoric ensemble available in LAMMPS. In order to obtain stochastic information of the configurational space, statistical data was collected by initializing the system using the Gaussian seed method, wherein initial atomic trajectories were selected at random from the Boltzmann distribution. Five simulation repetitions were performed at each testing condition, resulting in a reasonable sampling of statistical scatter (see Section 3.2). Stress was calculated as the spatial and temporal average of the per atom values using the virial theorem and strain (ϵ) was defined in engineering terms. For conversion to 3D stress values, the thickness of the graphene sheet was assumed to be 3.35 Å [16,17]. All simulations were conducted with a 1 fs timestep. This computational approach as well as simulation cell size has been validated through a comparative study against existing computational reports of pristine graphene strength [40,41]. Visualization of atomic topologies was achieved using the AtomEye atomistic configuration viewer [42].

3. Results and discussion

3.1. Quasi-intrinsic strength of defective graphene sheets

Although the failure initiation in defective graphene is thermally activated, tensile simulations conducted under very high strain rates may be considered to measure quasi-intrinsic strength at the prescribed temperature. Here we report the quasi-intrinsic tensile behavior of the topological point reconstructions through
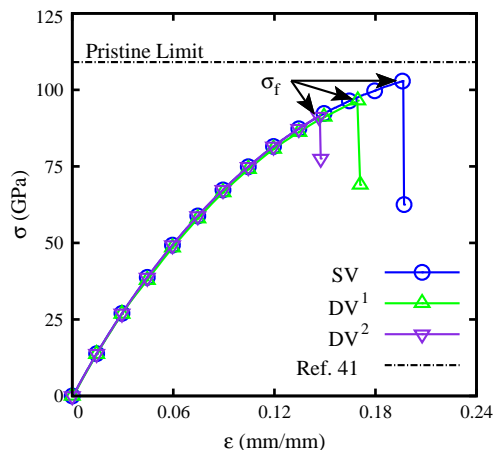
MD simulations and compare results against existing modeling data. Fig. 3 provides representative stress–strain curves for MD tensile simulations performed at 300 K and a strain rate ($\dot{\epsilon}$) of 10^9/s. Material failure was identified by a sudden drop in tensile stress and the fracture strength (σ_f) was then taken to be the maximum stress measured in the loading curve, as indicated in Fig. 3. Under these testing conditions, the SV defect was found to have the highest strength, whereas the DV^2 topological reconstruction was the weakest. This result is somewhat counterintuitive, as the SV and DV^1 reconstructions possessed higher potential energies in the defect core relative to the coordinated DV^2 structure. Furthermore, previous computational studies of polycrystalline graphene have shown that defective structures possessing a high density of heptagon–pentagon dipoles (as in the DV^2 case) exhibit near-pristine strength [34,40,43]. However, the periodic arrangement of dipoles in polycrystalline graphene imposes complementary tensile and compressive stress fields along grain boundaries [40]. Isolated heptagon–pentagon point defects do not experience the same lattice relaxation from overlapping stress fields as in line defects, which is likely the cause of the observed strength reduction in the DV^2 reconstruction.

Examination of the collected statistical results showed average fracture strengths of 100.5 ± 1.9, 95.7 ± 1.1, and 92.1 ± 1.5 GPa for the SV, DV^1, and DV^2 reconstructions respectively (see Fig. 4b), representing a decrease of 8–16% when compared to the fracture strength of pristine graphene (109 GPa) [41]. Error margins are reported here as 95% confidence intervals. Experimental atomic force microscopy nanoindentation tests as well as first-principles density functional theory calculations have placed the fracture strength of pristine graphene in the range of 100–130 GPa [16,17,40]. However, the loading configurations as well as the temperature and strain-rate conditions for these investigations were not consistent with the current study. The estimate in Ref. [41] was collected under identical loading conditions, and therefore served as the most direct comparison to the point reconstruction data. The influence of kinetic factors on weakening in defective graphene samples as well as the physical morphology of fracture processes are examined in subsequent sections.

3.2. Strain rate effects on the strength of defective graphene samples

Fig. 4a presents representative MD tensile results for the DV^2 defect at strain rates of 10^7 and 10^9/s. The fracture strength of the DV^2 samples was observed to decrease from 94 to 82 GPa, representing a strength drop of approximately 13% over the presented strain rate range. The collected statistics for strength measurements of the topological point reconstructions at each strain rate condition are presented in Fig. 4b. All MD data presented here was collected at a temperature of 300 K. While differences in fracture strengths were relatively minor at $\dot{\epsilon} = 10^9$/s (approximately 8 GPa), this range almost doubled to around 14 GPa at $\dot{\epsilon} = 5 \times 10^6$/s, where averaged values of 94.8 ± 1.2 (SV), 87.2 ± 2.5 (DV^1), and 80.7 ± 1.9 GPa (DV^2) were measured. The DV^2 defect was therefore found to be the most sensitive to strain rate effects, whereas the SV reconstruction was the most tolerant. The effect of strain rate on fracture stress in the sampled topological point reconstructions is qualitatively comparable to results reported by Sun et al. [21] for graphene nanoribbons with Stone–Wales defects. MD testing at strain rates lower than 5×10^6/s is not practical due to current limitations on computational power. It is expected that this trend in weakening continues to widen as strain rates approach magnitudes typical in experimental investigations of graphene. For instance, AFM nanoindentation is typically performed at strain rates of $\sim 10^0$/s [18].

The thermal activation theory of Eyring et al. [28] and the Arrhenius relationship may be extended to analytically predict
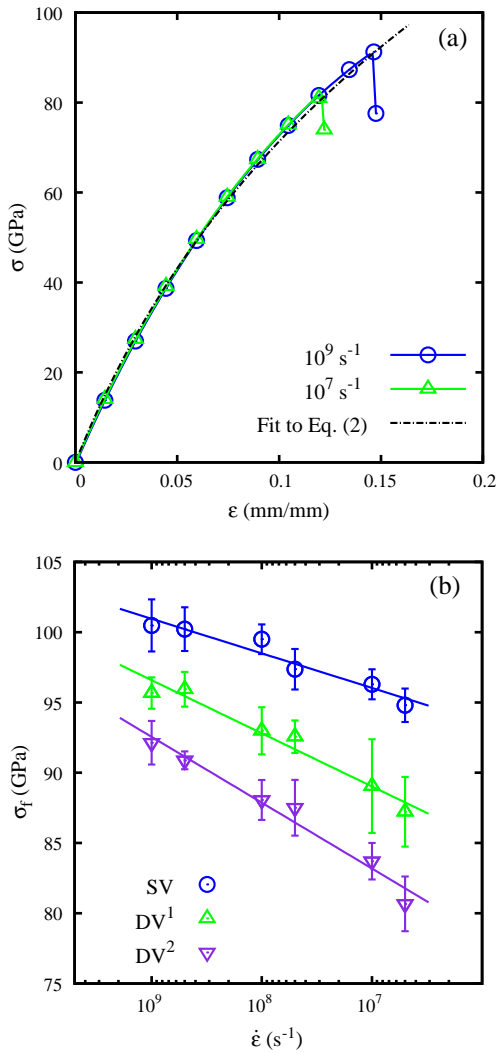

Fig. 3. MD tensile results for the topological point reconstructions at 300 K and a 10^9/s strain rate. Fracture strength (σ_f) was considered here to be the maximum measured stress, as indicated in the figure. The fracture strength of pristine graphene loaded in the zigzag orientation is provided for comparison [41].

Fig. 4. (a) Representative MD tensile results for the DV[2] defect at strain rates of 10^7 and 10^9/s. Eq. (2) is overlaid with the MD data using a = 82.89 GPa and b = 13.65. (b) The collected strengths of topological point reconstructions across all strain rate conditions. These results were fit to Eq. (3) yielding the energy barriers and activation volumes provided in Table 1. Based on Eq. (3), the predicted strengths of the topological point reconstructions were calculated and overlaid with the MD data, showing excellent agreement. The presented MD tensile data were collected at 300 K. Error bars represent a 95% confidence interval (n = 5).

the effects of strain rate on strength in defective systems over large timescales. The average lifetime to failure τ of a sample under stress σ and at temperature T undergoing N state transitions (*i.e.* failure propagation) is given by:

$$\tau = \frac{N\tau_o}{n_s} exp\left(\frac{\overline{E}_{eff} - V_a\sigma}{k_bT}\right) \qquad (1)$$

where $\tau_o \approx 0.1$ ps is the period of crystal vibrations [25,29], $N/n_s \approx 1$ is the ratio of state transitions to the number of sites available to undergo activation, $\overline{E}_{eff}$ is the average energy barrier resisting the fracture event, V_a is the activation volume, and k_b is the Boltzmann constant. In this weakest-link formulation, $\overline{E}_{eff}$ implicitly captures the effect of stress fields imposed by defects, which would lower the energy barrier of the fracture event as long as failure is observed to occur at the defect site. This approach has been validated in previous studies of defective graphene and carbon nanotubes [34,44]. Other analytical techniques such as Quantized Fracture Mechanics (QFM) [45] may also be implemented in energy

barrier analysis of defective graphene. However, this formulation requires precise knowledge of crack evolution geometry, as in the case of nano-cracks [25,29,30], and is therefore ideally suited for the analysis of single state transitions (see Section 3.5). Since fracture strengths were measured in a relatively narrow statistical range at each strain rate condition (Fig. 4b), $\overline{E}_{eff}$ nonetheless adequately captures the path-independent energy barrier.

In order to utilize Eq. (1) with strain-rate controlled MD tensile data, a time-dependent analytical expression for the stress–strain response of graphene was required. Following the methodology developed by Zhao and Aluru [29], the non-linear elastic response of graphene was captured using the following logarithmic relation:

$$\sigma(t) = a\ln(b\dot{\epsilon}t + 1) \qquad (2)$$

where a and b are constants fit from MD tensile data, and t is the time of the simulation. Least squares fitting of Eq. (2) to MD tensile data yielded a = 82.89 GPa and b = 13.65. As described in [29], Eq. (2) may be shown to reduce to a first-order form of $\sigma \approx ab\epsilon$, whereby the product ab yields 1.13 TPa, in good agreement with the experimentally measured first-order elastic modulus reported in [16]. Using the fitted values of a and b, Eq. (2) is overlaid with MD tensile data in Fig. 4a, showing excellent agreement. Since each of the topological point reconstructions represented a small area fraction of the MD simulation cell and therefore had only a marginal impact on elastic properties, a singular fit was used to describe the stress–strain response of all vacancy defects considered. Setting $\sigma = \sigma_f$, Eq. (2) may be substituted into Eq. (1) and application of the Bailey criterion [46] yields an explicit expression for the strain-rate sensitivity of the fracture process in the form of:

$$\sigma_f = \frac{ak_bT}{V_aa + k_bT}\left\{\frac{\overline{E}_{eff}}{k_bT} + \ln\left[\frac{Nb\dot{\epsilon}\tau_o}{n_s}\left(\frac{V_aa}{k_bT} + 1\right)\right]\right\} \qquad (3)$$

Further explanation and derivation of this formulation may be found in [29]. Fitting of the collected MD data presented in Fig. 4b yielded effective energy barriers and activation volumes (see Table 1) in the range of 1.25–2.5 eV and 2–3.8 Å^3, respectively, for each of the topological point reconstructions. In order to contextualize these results, the fitted values presented in Table 1 were compared to known parameters for pristine graphene, which may be considered as upper bound estimates for these variables. As previously reported, 4.93 eV [47] and 8.49 Å^3 [29] are the energy barrier and activation volume for fracture in pristine graphene. With respect to the pristine values, $\overline{E}_{eff}$ and V_a should be lower for defective systems as stresses arising from topological irregularities both reduce the required energy for crack formation and confine the fracture process to specific critical bonds. The calculated values of $\overline{E}_{eff}$ and V_a for the topological point reconstructions were substituted into Eq. (3) and the results are overlaid with MD data at 300 K in Figure 4b, showing excellent agreement.

In order to validate the fitted values for $\overline{E}_{eff}$ and V_a, Eq. (3) may be extended to analytically predict strengths at experimental strain rates (*e.g.* ∼10^0/s). Fig. 5 presents an extension of Eq. (3) for the topological point reconstructions to laboratory loading conditions. Due to strain rate effects, fracture strengths were found to substantially decrease across all the topological point

Table 1
The energy barriers and activation volumes to fracture in defective and pristine graphene samples.

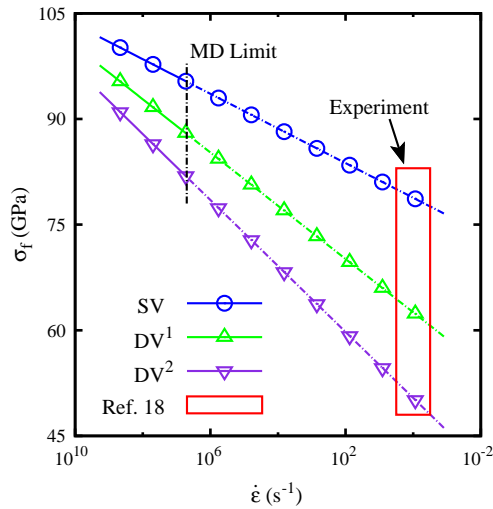| Defect	$\overline{E}_{eff}$ (eV)	V_a (Å^3)
SV	2.50	3.83
DV[1]	1.59	2.47
DV[2]	1.25	1.99
Pristine	4.93 [47]	8.49 [29]

Fig. 5. Extension of Eq. (3) to experimental loading rates for each of the topological point reconstructions at 300 K. Extrapolation beyond the MD range is indicated in dot-dashed stroke. These calculations were compared to existing experimental results for defective graphene from [18]. The predictions span the range of the experimental data, corroborating MD results.

Fig. 6. The collected MD strengths of the topological point reconstructions at different testing temperatures. MD tensile simulations were conducted at a strain rate of 10^9/s. Error bars represent the 95% confidence interval ($n = 5$). In some cases error bars fall within the marker perimeter.

reconstructions (T = 300 K). Specifically, the SV, DV^1, and DV^2 defects were calculated to weaken by 22% (101–79 GPa), 35% (97–63 GPa), and 46% (93–50 GPa), respectively, from strain rates of 10^9 to 10^0/s. Furthermore, the range in strengths between the SV and DV^2 reconstructions was found to widen considerably from 8 GPa at 10^9/s to 29 GPa at 10^0/s. From a weakest-link perspective, the DV^2 reconstructions are therefore expected to dictate the fracture strength of defective graphene at realistic loading conditions. Although a direct comparison to experimental measurements is not currently available, predictions from Eq. (3) provide a reasonable comparison to experimental studies of strength in polycrystalline graphene. For example, Rasool et al. [18] reported strengths of 48–83 GPa, which spans the range predicted by the current MD study and corroborates the results presented herein. It should be noted, however, that although point defects such as the DV^2 reconstruction are topologically similar to the heptagon–pentagon disclination dipoles which populate grain boundaries in polycrystalline graphene [8], their fracture strengths may only be approximately compared.

3.3. Influence of temperature on the fracture strength of defective graphene samples

The impact of temperature on the mechanical properties of defective graphene samples was examined in order to verify the comparative strengths observed in rate-controlled MD testing. Fig. 6 presents the results of MD simulations at temperatures of 1, 150, 300 and 450 K under a loading rate of 10^9/s. The strength of the SV reconstruction was found to decrease by 12% from 109.3 ± 0.2 to 96.6 ± 0.6 GPa at temperatures of 1 and 450 K respectively. Similarly, the DV^1 and DV^2 structures were observed to decrease by 15% (105.4 ± 1.2–89.5 ± 1.5 GPa) and 16% (103.7 ± 0.6–87.0 ± 2.5 GPa) respectively, over the same temperature range. The hierarchy of defect strength observed in the rate-controlled MD testing was therefore preserved when varying system temperature and weakening appears to follow a linear relationship across temperature space. This proportional behavior is expected from thermal activation theory and is captured analytically in the exponent of Eq. (1). The impact of temperature was not as drastic as the analytical predictions of strain rate effects on the mechanical properties of defective graphene. Additionally,
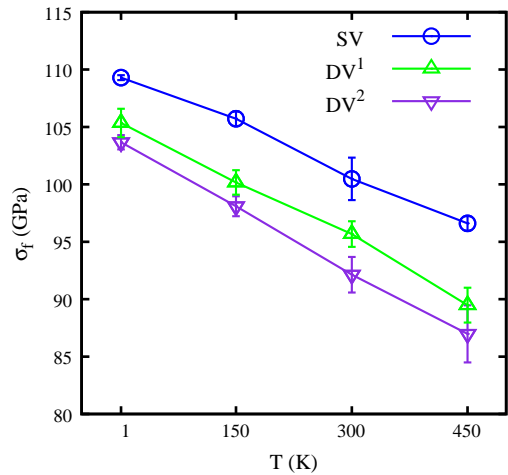
each topological point reconstruction exhibited a similar degree of strength loss. Nonetheless, weakening is expected to be exacerbated when measured across larger temperature ranges and when sampled in combination with lower strain rates.

3.4. Crack morphology and progressive failure in defective graphene samples

From the presented MD studies and analytical considerations, the SV defect was found to be the strongest of the studied topological point reconstructions. This result is somewhat counterintuitive since the DV^2 defect appeared to be the lowest energy (as shown in Fig. 2). In order to understand the physical rationale underpinning failure phenomena, the evolution of crack morphology during deformation was examined. The presented atomic snapshots of failure were collected for tensile simulations performed at 300 K and a strain rate of 10^9/s. The mechanisms illustrated in the subsequent section were observed at all testing conditions considered in this study. Fig. 7 presents representative snapshots of the SV reconstruction undergoing progressive failure. It was observed that during heating in MD testing the bond shared between the pentagon and irregular-nonagon spontaneously cleaved without applied loading, forming a irregular-dodecagon. This topology is illustrated in Fig. 7a. After this initial break, the SV defect remained stable until approximately 15% strain, where an under-coordinated atom experienced bond rotation, subsequently creating an additional pentagon defect (Fig. 7b). Further loading led to a multiplicity of topological defects, creating another pentagon reconstruction (Fig. 7c) and ultimately causing fracture in the surrounding hexagonal graphene lattice (Fig. 7d). Once the crack propagated into the surrounding graphene, brittle fracture was observed to occur rapidly. The progression of the critical crack was observed to occur over approximately 4% strain in the SV reconstruction, which is somewhat surprising for a brittle material. This finding is in contrast to a previous computational report of supersonic crack propagation in pristine graphene [48]. One interpretation is that multiple bond rotations allow a degree of deformation accommodation in the SV reconstruction, whereby atomic-scale movements are facilitated by the high mobility of under-coordinated atoms in the defect core. The multiplicity of pentagon defects hinders crack growth and permits material survival at increased loadings. Conversely, the fully-coordinated pristine hexagonal unit cell may not easily undergo bond rotations, leading instead to crack
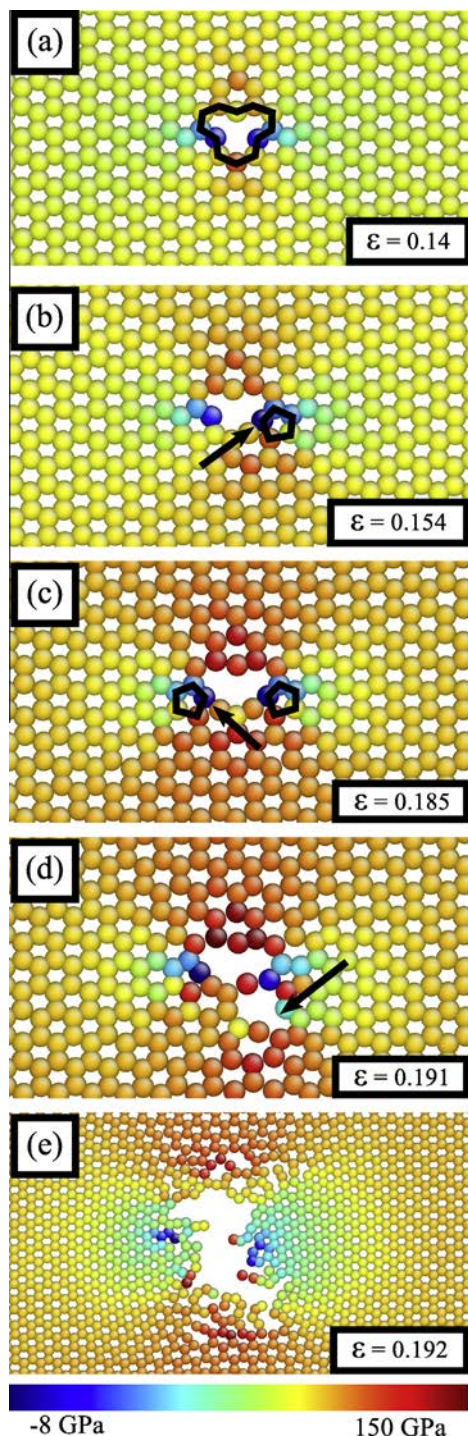
Fig. 7. Progressive failure in the SV reconstruction (T = 300 K, $\dot{\epsilon}$ = 10^9/s). Snapshots were taken at ϵ = 0.14 (a), 0.154 (b), 0.185 (c), 0.191 (d), and 0.192 (e). Bond rotations at under-coordinated atoms in the dodecagon irregular-dodecagon were observed to accommodate deformation (b and c) and create new pentagon defects. This behavior delayed critical cracking until bonds in the hexagonal lattice were broken (d), leading to rapid fracture (e). The colormap shows per atom stress. (For interpretation of the references to color in this figure legend, the reader is referred to the web version of this article.)

Fig. 8. Snapshots of failure in the DV^1 reconstruction (T = 300 K, $\dot{\epsilon}$ = 10^9/s). At ϵ = 0.12 (a), the DV^1 defect possessed four under-coordinated atoms which permitted bond rotations at ϵ = 0.125 (b), 0.135, and 0.15 to accommodate deformation. In this manner, bond rotations served as a competing deformation mechanism to brittle fracture, delaying material failure until a critical crack initiated in the hexagonal graphene lattice just prior to ϵ = 0.166 (e). The colormap shows per atom stress. (For interpretation of the references to color in this figure legend, the reader is referred to the web version of this article.)

propagation and rapid fracture. Bond rotation in graphene has been previously observed in computational studies of Stone–Wales formation [25] as well as failure propagation in elliptical nano-cracks [31], but has not been reported for the reconstructed point defects.
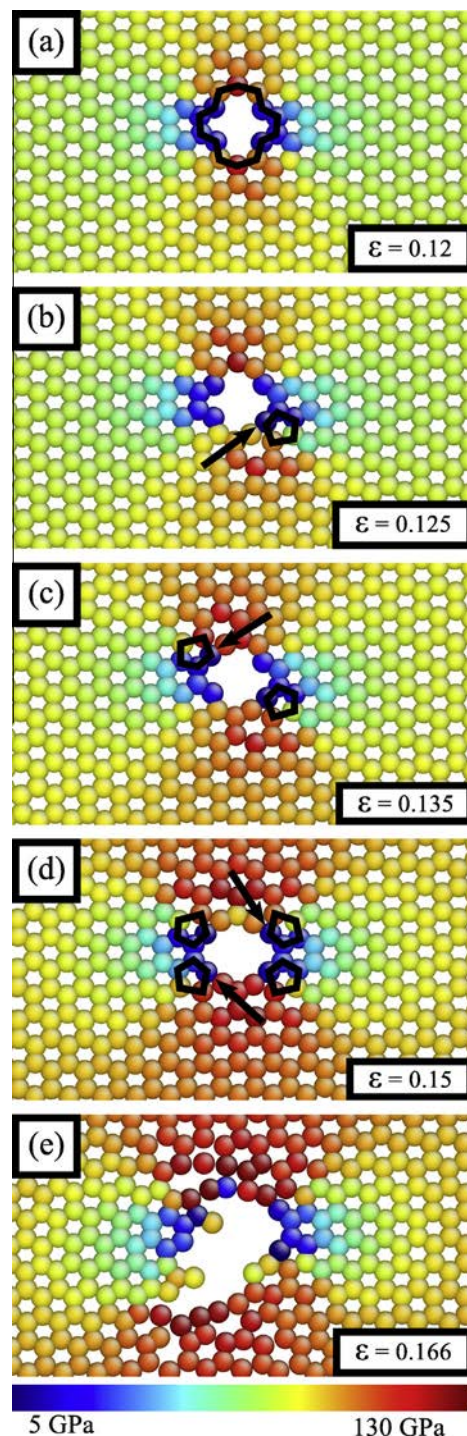
In comparison to the SV defect, similar failure behavior was observed in the DV^1 reconstruction. Fig. 8 presents progressive snapshots of failure in the DV^1 defect. As with the SV defect, the initial high-energy bonds shared by the pentagon and octagon structures were cleaved by thermal effects to yield under-coordinated atoms and the DV^1 appeared as a nano-void in the

form of a irregular-tetrakaidecagon. Upon further loading, bond rotations created pentagon defects in a manner similar to the SV reconstruction (Fig. 8b–d, effectively enlarging the nano-void until rapid fracture occurred in the hexagonal graphene lattice (Fig. 8e). With respect to the SV defect, the large void and stress concentrations created by the tetrakaidecagon (as opposed to the dodecagon in the SV reconstruction), encouraged failure initiation at a lower stress. Conversely, the geometrically larger tetrakaidecagon possessed more under-coordinated atoms and thereby permitted additional pentagon defects to form, potentially leading to increased deformation accommodation relative to the SV structure.

In contrast to the SV and DV[1] reconstructions, the DV[2] defect appeared to be much more sensitive to cracking and flaw initiation. Fig. 9 presents snapshots of the DV[2] during fracture. The DV[2] defect was observed to retain full coordination until approximately 15% strain (Fig. 9a). This value is notably higher than the applied strain for initial bond rotation of the DV[1] defect. Upon crack initiation in the DV[2] reconstruction (Fig. 9b), rapid fracture followed almost immediately (Fig. 9c). Therefore, although the DV[2] defect survived as a fully coordinated reconstruction to strain levels comparable to the SV defect, it exhibited significantly lower flaw tolerance.

3.5. Flaw tolerance of the defective graphene samples

In order to quantify the degree of deformation accommodation during failure progression in each of the topological point reconstructions, the averaged flaw tolerances were calculated and provided in Fig. 10 ($T = 300$ K, $\dot{\epsilon} = 10^9$/s). Flaw tolerance (ϵ_{ft})
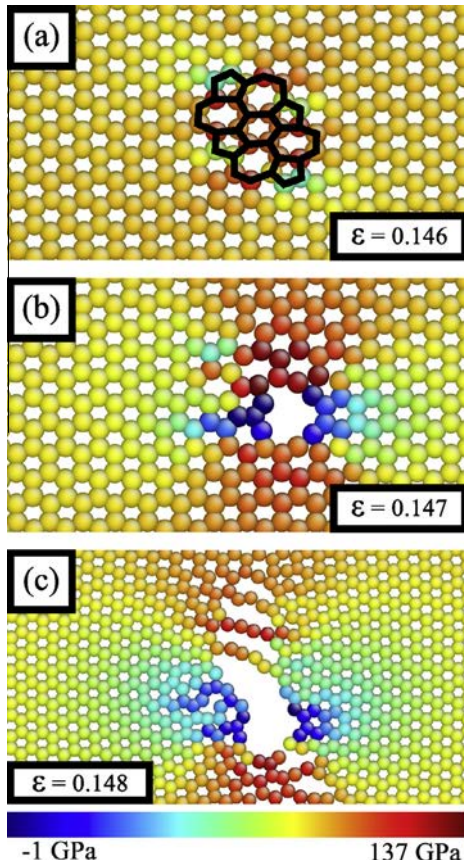

Fig. 9. Rapid fracture in the DV[2] reconstruction ($T = 300$ K, $\dot{\epsilon} = 10^9$/s). A critical crack initiated within the defect structure between $\epsilon = 0.146$ (a) and $\epsilon = 0.147$ (b). Ultimate failure proceeded quickly, with fracture having progressed into the hexagonal graphene lattice at $\epsilon = 0.148$ (c). The colormap shows per atom stress. (For interpretation of the references to color in this figure legend, the reader is referred to the web version of this article.)
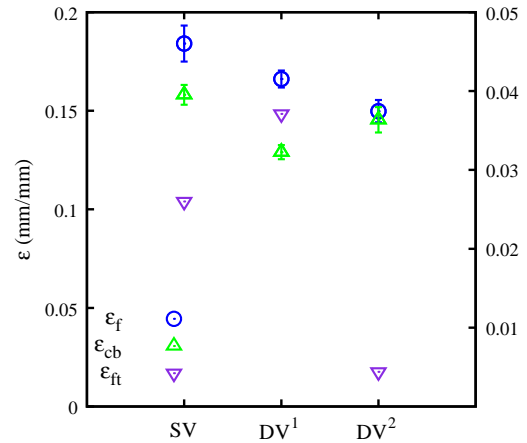

Fig. 10. Measurements of flaw tolerance for the topological point reconstructions at 300 K and a strain rate of 10[9]/s. Flaw tolerance (ϵ_{ft}) was defined as the difference between the strain at failure (ϵ_f) and the strain at failure initiation (ϵ_{cb}). The DV[2] reconstruction was observed to possess the least flaw tolerance which was a result of its lack of under-coordinated atoms. ϵ_{ft} is plotted with reference to the secondary ordinate. Error bars represent the 95% confidence interval ($n = 5$).

was defined in this context to be the difference between the strain at ultimate failure (ϵ_f) and the strain of the initial failure event (ϵ_{cb}). Under this definition, ϵ_{cb} may represent the strain of critical crack initiation in the DV[2] defect as well as the first instance of bond rotation in the SV and DV[1] topological reconstructions. As observed from the snapshots of graphene fracture, the DV[1] reconstruction was found to have the highest tolerance to cracking ($\epsilon_{ft} = 0.037$), but simultaneously the lowest ϵ_{cb} (0.129 ± 0.004). In comparison, the SV defect exhibits a similar degree of flaw tolerance ($\epsilon_{ft} = 0.026$) and a larger ϵ_{cb} (0.158 ± 0.005). On the other hand, the DV[2] possesses almost an insignificant amount of flaw tolerance ($\epsilon_{ft} = 0.004$).

Under the assumption of perfectly brittle fracture, QFM calculations were performed to further contextualize flaw tolerance in the SV and DV[1] topological reconstructions. Taking the deformed topologies of the SV and DV[1] defects prior to bond rotation as nano-cracks (*i.e.* the topologies in Figs. 7a and 8a), QFM was implemented to predict the instantaneous brittle fracture strength of these specific topological states under Mode I loading. Assuming that finite plate effects are minimized due to the relatively large simulation cell size, the brittle fracture stress of a crack with radius ρ and length $2a$ is described by the following relation:

$$\sigma_f = \sigma_p \sqrt{\frac{1 + \rho/2a_o}{1 + 2a/a_o}} \tag{4}$$

where a_o is the crack quantum (0.28 nm [30]), and σ_p is the fracture strength of pristine graphene. The crack geometry parameters for
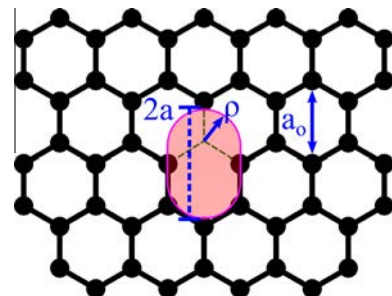

Fig. 11. The assumed crack geometry of the SV defect for QFM calculations of fracture strength under Mode I loading. The geometric parameters are defined in text (Section 3.5).

the SV case are illustrated schematically in Fig. 11. Assuming a pristine fracture strength of 109 GPa at 300 K, the fracture strength of the SV ($\rho \approx 0.12$ nm, $2a \approx 0.43$ nm) and DV^1 ($\rho \approx 0.12$ nm, $2a \approx 0.71$ nm) defects were calculated as 76 ($\approx 0.7\sigma_p$) and 65 GPa ($\approx 0.6\sigma_p$), respectively. These predictions of σ_f are in agreement with calculations performed by Dewapriya et al. [30] for zigzag nano-cracks in graphene. Taking the $\dot{\epsilon} = 10^9$/s MD tensile data as instantaneous, comparatively, the SV and DV^1 were found to be significantly stronger than QFM calculations (100.5 ± 1.9 and 95.7 ± 1.1, respectively). In this regard, bond rotation therefore permitted flaw tolerance and enabled a deformation accommodation mechanism that suppressed brittle fracture. An equivalent QFM calculation cannot be directly performed for the DV^2 topological reconstruction as the defect is fully coordinated up to fracture. However, consideration of the critical heptagon reconstruction (Fig. 9b) as a pseudo nano-crack yielded a QFM Mode I brittle fracture strength of ≈ 91 GPa. This value is in excellent agreement with the collected MD fracture strength measurements (92.1 ± 1.5 GPa) and reinforces the observation of poor flaw tolerance in the DV^2 topological reconstruction.

In a general sense, the differences observed between each of the sampled topological point reconstructions were physically linked to the number of deformation-accommodating bond rotations that may be initiated within the flaw. The ability of atoms to undergo bond rotations was found to be related to the presence of under-coordinated atoms within the topological point reconstructions. Under-coordination in the topological structure surrounding the defect core permitted a less-constrained motion of atoms, which served as a competing deformation mechanism to rapid brittle fracture. One consequence of this observation is that, although higher densities of defects (e.g. the SV reconstruction) may cause weakening in pristine graphene, some configurations of these reconstructions could hinder critical cracking and be beneficial to material ductility. It should be noted, however, that the bond rotation effects observed in this study were sensitive to loading configuration. MD tensile studies performed under armchair or biaxial loadings may not engage the same deformation mechanisms as the movement of undercoordinated atoms is more restricted under some loading configurations. Additionally, recent MD studies have highlighted the impact of defect density on the mechanical properties of graphene [23,49]. A detailed investigation of the interactions of multiple defects undergoing bond rotations may therefore provide further insight into the deformation behavior of defective graphene. In this regard, defect engineering may serve as a route for tuning of the fracture toughness and ultimate failure strain in graphene.

4. Conclusions

The comparative strengths of common topological point reconstructions in graphene were examined with MD tensile simulations. In order to provide a meaningful estimate of realistic strengths at experimental loading rates and circumvent the traditional limitations on direct MD studies, strain rate effects were considered through calculation of energy barriers resisting fracture. Results indicated that, although the under-coordinated SV and DV^1 reconstructions possessed higher potential energies, they were found to be stronger than the DV^2 defect under all testing protocols. Additionally, the DV^2 structure was found to be more sensitive to strain rate effects than the other topological reconstructions. Defective graphene samples were observed to weaken significantly when strength calculations were extended to experimental loading rates. Analytical predictions of strength for the topological point reconstructions at quasi-static strain rates were found to agree well with available experimental reports. A similar MD study with varied system temperature preserved the strength trends established during analysis of strain rate effects. Physically, the differences in strengths of the topological point reconstructions were found to be a result of flaw tolerance in the underlying defect structure. The DV^2 defect was found to be very sensitive to critical cracking, whereas the SV and DV^1 reconstructions were found to posses significant flaw tolerance. Specifically, the SV and DV^1 reconstructions were observed to undergo a series of bond rotations at the under-coordinated atoms prior to critical cracking, which permitted a degree of deformation accommodation that suppressed rapid fracture. Further investigations of the effects of loading and defect density may provide additional insight into the deformation behavior of defective graphene.

References

[1] K.S. Kim, Y. Zhao, H. Jang, S.Y. Lee, J.M. Kim, K.S. Kim, J.-H. Ahn, P. Kim, J.-Y. Choi, B.H. Hong, Nature 457 (7230) (2009) 706–710, http://dx.doi.org/10.1038/nature07719.

[2] A. Reina, X. Jia, J. Ho, D. Nezich, H. Son, V. Bulovic, M.S. Dresselhaus, J. Kong, Nano Lett. 9 (1) (2009) 30–35, http://dx.doi.org/10.1021/nl801827v.

[3] S. Bae, H. Kim, Y. Lee, X. Xu, J.-S. Park, Y. Zheng, J. Balakrishnan, T. Lei, H.R. Kim, Y.I. Song, Y.-J. Kim, K.S. Kim, B. Ozyilmaz, J.-H. Ahn, B.H. Hong, S. Iijima, Nat. Nanotechnol. 5 (8) (2010) 574–578, http://dx.doi.org/10.1038/nnano.2010.132.

[4] X. Li, W. Cai, J. An, S. Kim, J. Nah, D. Yang, R. Piner, A. Velamakanni, I. Jung, E. Tutuc, S.K. Banerjee, L. Colombo, R.S. Ruoff, Science 324 (5932) (2009) 1312–1314, http://dx.doi.org/10.1126/science.1171245.

[5] M.P. Levendorf, C.S. Ruiz-Vargas, S. Garg, J. Park, Nano Lett. 9 (12) (2009) 4479–4483, http://dx.doi.org/10.1021/nl902790r.

[6] A. Hashimoto, K. Suenaga, A. Gloter, K. Urita, S. Iijima, Nature 430 (7002) (2004) 870–873, http://dx.doi.org/10.1038/nature02792.1.

[7] P.Y. Huang, C.S. Ruiz-Vargas, A.M. van der Zande, W.S. Whitney, M.P. Levendorf, J.W. Kevek, S. Garg, J.S. Alden, C.J. Hustedt, Y. Zhu, J. Park, P.L. McEuen, D.A. Muller, Nature 469 (7330) (2011) 389–392, http://dx.doi.org/10.1038/nature09718.

[8] K. Kim, Z. Lee, W. Regan, C. Kisielowski, M.F. Crommie, A. Zettl, ACS Nano 5 (3) (2011) 2142–2146, http://dx.doi.org/10.1021/nn1033423.

[9] J.C. Meyer, C. Kisielowski, R. Erni, M.D. Rossell, M.F. Crommie, A. Zettl, Nano Lett. 8 (11) (2008) 3582–3586, http://dx.doi.org/10.1021/nl801386m.

[10] J. Kotakoski, A.V. Krasheninnikov, U. Kaiser, J.C. Meyer, Phys. Rev. Lett. 106 (10) (2011) 105505, http://dx.doi.org/10.1103/PhysRevLett.106.105505.

[11] F. Banhart, J. Kotakoski, A.V. Krasheninnikov, ACS Nano 5 (1) (2011) 26–41, http://dx.doi.org/10.1021/nn102598m.

[12] A. El-Barbary, R. Telling, C. Ewels, M. Heggie, P. Briddon, Phys. Rev. B 68 (14) (2003) 144107, http://dx.doi.org/10.1103/PhysRevB.68.144107.

[13] J.-M. Leyssale, G.L. Vignoles, J. Phys. Chem. C 118 (15) (2014) 8200–8216, http://dx.doi.org/10.1021/jp501028n.

[14] A. Krasheninnikov, P. Lehtinen, A. Foster, R. Nieminen, Chem. Phys. Lett. 418 (1–3) (2006) 132–136, http://dx.doi.org/10.1016/j.cplett.2005.10.106.

[15] Y. Kim, J. Ihm, E. Yoon, G.-D. Lee, Phys. Rev. B 84 (7) (2011) 75445, http://dx.doi.org/10.1103/PhysRevB.84.075445.

[16] C. Lee, X. Wei, J.W. Kysar, J. Hone, Science 321 (5887) (2008) 385–388, http://dx.doi.org/10.1126/science.1157996.

[17] G.-H. Lee, R.C. Cooper, S.J. An, S. Lee, A. van der Zande, N. Petrone, A.G. Hammerberg, C. Lee, B. Crawford, W. Oliver, J.W. Kysar, J. Hone, Science 340 (6136) (2013) 1073–1076, http://dx.doi.org/10.1126/science.1235126.

[18] H.I. Rasool, C. Ophus, W.S. Klug, A. Zettl, J.K. Gimzewski, Nat. Commun. 4 (2013) 2811, http://dx.doi.org/10.1038/ncomms3811.

[19] C.S. Ruiz-Vargas, H.L. Zhuang, P.Y. Huang, A.M. van der Zande, S. Garg, P.L. McEuen, D.A. Muller, R.G. Hennig, J. Park, Nano Lett. 11 (6) (2011) 2259–2263, http://dx.doi.org/10.1021/nl200429f.

[20] A. Zandiatashbar, G.-H. Lee, S.J. An, S. Lee, N. Mathew, M. Terrones, T. Hayashi, C.R. Picu, J. Hone, N. Koratkar, Nat. Commun. 5 (2014) 3186, http://dx.doi.org/10.1038/ncomms4186.

[21] Y.J. Sun, F. Ma, D.Y. Ma, K.W. Xu, P.K. Chu, J. Phys. D: Appl. Phys. 45 (30) (2012) 305303, http://dx.doi.org/10.1088/0022-3727/45/30/305303.

[22] J.R. Xiao, J. Staniszewski, J.W. Gillespie, Mater. Sci. Eng.: A 527 (3) (2010) 715–723, http://dx.doi.org/10.1016/j.msea.2009.10.052.

[23] L. Xu, N. Wei, Y. Zheng, Nanotechnology 24 (50) (2013) 505703, http://dx.doi.org/10.1088/0957-4484/24/50/505703.

[24] L. He, S. Guo, J. Lei, Z. Sha, Z. Liu, Carbon 75 (2014) 124–132, http://dx.doi.org/10.1016/j.carbon.2014.03.044.

[25] M.C.C. Wang, C. Yan, L. Ma, N. Hu, M.W.W. Chen, Comput. Mater. Sci. 54 (2012) 236–239, http://dx.doi.org/10.1016/j.commatsci.2011.10.032.

[26] R. Ansari, S. Ajori, B. Motevalli, Superlattices Microstruct. 51 (2) (2012) 274–289, http://dx.doi.org/10.1016/j.spmi.2011.11.019.

[27] J.A. Baimova, L. Bo, S.V. Dmitriev, K. Zhou, A.A. Nazarov, Europhys. Lett. 103 (4) (2013) 46001, http://dx.doi.org/10.1209/0295-5075/103/46001.

[28] G. Halsey, H.J. White, H. Eyring, Text. Res. J. 15 (9) (1945) 295–311, http://dx.doi.org/10.1177/004051754501500901.

[29] H. Zhao, N.R. Aluru, J. Appl. Phys. 108 (2010) 064321, http://dx.doi.org/10.1063/1.3488620.

[30] M.A.N. Dewapriya, R.K.N.D. Rajapakse, A.S. Phani, Int. J. Fract. 187 (2) (2014) 199–212, http://dx.doi.org/10.1007/s10704-014-9931-y.

[31] S.S. Terdalkar, S. Huang, H. Yuan, J.J. Rencis, T. Zhu, S. Zhang, Chem. Phys. Lett. 494 (4–6) (2010) 218–222, http://dx.doi.org/10.1016/j.cplett.2010.05.090.

[32] A. Cao, Y. Yuan, Appl. Phys. Lett. 100 (21) (2012) 211912, http://dx.doi.org/10.1063/1.4722786.

[33] L. Yi, Z. Yin, Y. Zhang, T. Chang, Carbon 51 (2013) 373–380, http://dx.doi.org/10.1016/j.carbon.2012.08.069.

[34] M. Daly, C. Veer Singh, J. Appl. Phys. 115 (22) (2014) 223513, http://dx.doi.org/10.1063/1.4883190.

[35] R. Dettori, E. Cadelano, L. Colombo, J. Phys. Condens. Matter: An Inst. Phys. J. 24 (10) (2012) 104020, http://dx.doi.org/10.1088/0953-8984/24/10/104020.

[36] J. Zhao, H. Zeng, J. Wei, B. Li, D. Xu, Phys. Lett. A 378 (4) (2014) 416–420, http://dx.doi.org/10.1016/j.physleta.2013.11.037.

[37] L. Wu, T. Hou, Y. Li, K.S. Chan, S.-T. Lee, J. Phys. Chem. C 117 (33) (2013) 17066–17072, http://dx.doi.org/10.1021/jp405130c.

[38] S. Plimpton, J. Comput. Phys. 117 (June 1994) (1995) 1–42.

[39] S.J. Stuart, A.B. Tutein, J.A. Harrison, J. Chem. Phys. 112 (14) (2000) 6472, http://dx.doi.org/10.1063/1.481208.

[40] Y. Wei, J. Wu, H. Yin, X. Shi, R. Yang, M. Dresselhaus, Nat. Mater. 11 (9) (2012) 759–763, http://dx.doi.org/10.1038/NMAT3370.

[41] M.A.N. Dewapriya, R.K.N.D. Rajapakse, J. Appl. Mech. 81 (8) (2014) 081010, http://dx.doi.org/10.1115/1.4027681.

[42] J. Li, Model. Simulat. Mater. Sci. Eng. 0393 (03) (2003) 173–177.

[43] R. Grantab, V.B. Shenoy, R.S. Ruoff, Science 330 (6006) (2010) 946–948, http://dx.doi.org/10.1126/science.1196893.

[44] C. Wei, K. Cho, D. Srivastava, Phys. Rev. B 67 (11) (2003) 115407, http://dx.doi.org/10.1103/PhysRevB.67.115407.

[45] N.M. Pugno, R.S. Ruoff, Philos. Mag. 84 (27) (2004) 2829–2845, http://dx.doi.org/10.1080/14786430412331280382.

[46] J. Bailey, Glass Ind. 20 (21) (1939) 94.

[47] D.W. Brenner, O.A. Shenderova, J.A. Harrison, S.J. Stuart, B. Ni, S.B. Sinnott, J. Phys.: Condens. Matter 14 (4) (2002) 783–802, http://dx.doi.org/10.1088/0953-8984/14/4/312.

[48] B. Zhang, G. Yang, H. Xu, Phys. B: Condens. Matter 434 (2014) 145–148, http://dx.doi.org/10.1016/j.physb.2013.11.027.

[49] B. Mortazavi, S. Ahzi, Thermal conductivity and tensile response of defective graphene: a molecular dynamics study, Carbon 63 (2013) 460–470, http://dx.doi.org/10.1016/j.carbon.2013.07.017.